Robust and Fast 3D Saliency Mapping for Industrial Modeling Applications

Gerasimos Arvanitis⬤, and Aris S. Lalos⬤, *Senior Member, IEEE*, and Konstantinos Moustakas⬤, *Senior Member, IEEE*

Abstract—New generation 3D scanning technologies are expected to create a revolution at the Industry 4.0, facilitating a large number of virtual manufacturing tools and systems. Such applications require the accurate representation of physical objects and/or systems achieved through saliency estimation mechanisms that identify certain areas of the 3D model, leading to a meaningful and easier to analyze representation of a 3D object. 3D saliency mapping is, therefore, guiding the selection of feature locations and is adopted in a large number of low-level 3D processing applications including denoising, compression, simplification and registration. In this work, we propose a robust and fast method for creating 3D saliency maps that accurately identifies sharp and small scale geometric features in various industrial 3D models. An extensive experimental study using a large number of 3D scanned and CAD models, verifies the effectiveness of the proposed method as compared to other recent and relevant approaches despite the constraints posed by complex geometry patterns or the presence of noise.

Index Terms—3D Mesh saliency mapping, industrial modeling & applications, spectral & geometric analysis for vertex saliency.

I. Introduction

Visual computing technologies play an important role in several manufacturing tasks. Particularly nowadays, their role is crucial due to the new Industry 4.0 applications including manufacturing inspection [1], quality control [2], reverse engineering [3], digital twin [4] as well as autonomous repair operations. While the use of this new type of applications will expand, the number of the digital 3D models will be also increased, resulting in the interest for more accurate 3D model processing.

The resolution and accuracy of the modern 3D scanners are constantly increasing, making them even more attractive in several vision-based manufacturing tasks, allowing the accurate generation of dynamic virtual representations of physical objects which are then used for inspection. Inspecting the parts and repairing the damages or degradations are very basic tasks

for many engineering or manufacturing products. More specifically, surface defect inspection is of primary importance for engineering part quality inspection, since surface defects affect not only the appearance of parts, but also their functionality, efficiency and stability. This task mostly depends on human visual inspection by skilled inspectors. Human visual inspection is costly, labor-intensive, time-consuming, and prone to errors due to inspectors lack of experience or fatigue, bad environmental conditions, etc. Hence automatic inspection of the surfaces using computational techniques, which is faster, more consistent and robust, is highly desired [5]. We are motivated by the fact that there are a lot of new-era industrial applications that require the digitization of physical objects or systems (e.g., inspection, digital twin, industry 4.0, quality control, reverse engineering, etc.,) creating or using already scanned 3D objects. However, this digitized information is massive and raw, leading to the need of new essential and meaningful identification of features that will facilitate robust processing in various applications. These facts stress the need to focus on the development of computational models of visual attention, whose well-known outcomes are the saliency maps. Saliency maps are compact 3D representations, generated by simplifying, annotating and/or changing the representation of a physical object/system giving more emphasis to geometrically meaningful parts. The salient features also typically satisfy important requirements such as scaling, rotation, resolution invariance that can simplify industrial processes. In this work, we focus on providing a method for the accurate extraction of a meaningful 3D saliency mapping ideally suited for industrial 3D models. More specifically, the contributions of the proposed approach can be summarized as follows:

- designed to use both normals and guided normals, depending on the application. Guided normals provide more robust saliency mapping in cases of meshes affected by scanning noise and imperfections where other methods fail.
- combines the benefits of a spectral and a geometric approach in a single unified approach.
- exploits both local and global information of a model. In other words, the spectral method and the rows of the coherent matrix $\mathbf{E}$ enclose local information while the columns of the coherent matrix $\mathbf{E}$ encloses global information corresponding to larger patches.
- use the same configuration parameters independently of the input values for any model, making it 3D model

agnostic, without the need for further modification.

- has low-computational complexity, especially in comparison with other spectral methods that use the connectivity information of a model.
- It can be ideally used in applications related to industrial 3D models which have some special geometric characteristics (e.g., intense corners and edges) or have been affected by complex noise patterns.
- It is easily adaptive and can be efficiently adopted both by low-level applications (e.g., denoising, compression, registration, etc.), as a pre-processing step and/or by high-level industrial applications (e.g., maintenance, inspection, quality control, digital twin technologies, etc.)
- An extensive performance assessment using a large collection of different industrial 3D models, clearly shows the robustness of our method as compared to other approaches.

The rest of this paper is organized as follows: Section 2 presents state-of-the-art methods and related work. Section 3 presents some basic definitions and preliminaries. Section 4 describes in detail the work-flow of the proposed method and we show how our method can be used in a variety of actual industrial applications. Section 5 presents the experimental results and evaluation in comparison with other methods. Section 6 draws the conclusions of our method.

II. RECENT WORKS

Visual saliency is a subjective perception cue that differentiates a region from others and immediately attracts human attention [6]. The human visual system (HVS) is evolved to automatically detect salient regions over the entire field of view [7]. It is firstly attracted by the most representative salient elements and then the visual attention is transferred to other regions [8]. Most of the existing methods try to simulate the way that the human perceptual system works, giving more emphasis to what the human brain assumes as salient information. Nevertheless, what a human assumes as a salient feature may vary from what computational methods assume as salient. On the other hand, in industrial applications, simple geometry is usually more common and useful compared to complex surfaces of high spatial frequency that would trigger human visual attention. Wei *et al.* [9] presented a 3D saliency mapping mechanism using the curvature co-occurrence histogram, following similar steps with the method proposed in [10] for extracting salient image features. Tao *et al.* [11] proposed an entropy-based saliency approach using the entropy of the normals to depict the local changes in a region. Song *et al.* [12] proposed a method which incorporates global considerations by making use of spectral attributes. An *et al.* [13] proposed a hybrid saliency taking into account both color and geometric information. Nouri *et al.* [14] proposed a saliency-based metric for the evaluation of the quality between an original and a distorted 3D mesh comparing the structural information. They also [15] proposed a saliency method, using a local vertex descriptor that is used as a basis for similarity measurement and integrated into weighted multi-scale saliency

features. Zhao *et al.* [16] proposed a saliency detection method by diffusing a shape index field with a non-local means filter. Their algorithm generates a random center-surround operator to create a saliency map and use the Retinex theory to improve the saliency map. Wu *et al.* [17] proposed a 3D saliency map estimation considering both local contrast and global rarity. There are also many other methods that estimate a saliency mapping but with a completely different way. For example, the salient mapping of method [18], might be excellent for tactile-focused applications, is however, far from acceptable if applied in industrial applications like the ones demonstrated. Authors in [19] detect salient regions on the mesh based on the multi-scale Laplacian fairing results in order to use them for head pose estimation. What they assume as a salient region in their application is significantly different to we assume as salient features in our application. The authors in [20] try to automatically find landmark buildings in a city using a Context-dependency saliency mapping. In [21], the authors propose a saliency detection algorithm for large-scale colored 3D point clouds, which exploits geometric features and color features together to estimate the saliency in colored point clouds.

A major drawback of the aforementioned methods is that their robustness is significantly deteriorated when applied to scanned 3D models that have been affected by noise, outliers or missing parts. Additionally, most of these works provide only visual maps to show their effectiveness and none of them have been used and evaluated in real industrial applications.

III. PRELIMINARIES

In this section, we present the basic definitions and preliminaries which are necessary for the complete understanding of our assumptions.

A. Basic Definitions of 3D Meshes

In this work, we use triangle meshes $\mathcal{M}$ consisting of n vertices $\mathbf{v}$ and n_f faces f. A vertex $\mathbf{v}_i$ is represented by Cartesian coordinates, denoted by $\mathbf{v}_i = [x_i,\ y_i,\ z_i]^T$, $\forall\ i = 1, \cdots, n$, and a face $f_j = \{\mathbf{v}_{j1}\ \mathbf{v}_{j2}\ \mathbf{v}_{j3}\}$ is represented by its centroid $\mathbf{c}_j = (\mathbf{v}_{j1} + \mathbf{v}_{j2} + \mathbf{v}_{j3})/3$ and the outward unit normal $\mathbf{n}_{c_i} = \frac{(\mathbf{v}_{j2}-\mathbf{v}_{j1})\times(\mathbf{v}_{j3}-\mathbf{v}_{i1})}{\|(\mathbf{v}_{j2}-\mathbf{v}_{j1})\times(\mathbf{v}_{j3}-\mathbf{v}_{j1})\|}$, $\forall\ j = 1, \cdots, n_f$.

B. Robust Principal Component Analysis (RPCA)

RPCA has been used in order to decompose a observed measurement $\mathbf{E}$ into a low-rank matrix $\mathbf{L}$ representing the real data and a sparse matrix $\mathbf{S}$ representing the noisy data by solving: $\arg\min_{\mathbf{L},\mathbf{S}} \|\mathbf{L}\|_* + \lambda\|\mathbf{S}\|_1$, s.t. $\mathbf{L} + \mathbf{S} = \mathbf{E}$, where $\|\mathbf{L}\|_*$ is the nuclear norm of a matrix $\mathbf{L}$ (i.e, $\sum_i \sigma_i(\mathbf{L})$ is the sum of the singular values of $\mathbf{L}$). Despite the effectiveness that some works [22], [23] have presented in the past, their execution times need improvement. The computational complexity is a crucial issue, especially for use in industrial applications. We handle this convex problem using a very fast approach, as described in [24], according to:

$$\arg\min_{\mathbf{L},\mathbf{S}} \frac{1}{2}\|\mathbf{L} + \mathbf{S} - \mathbf{E}\|_F + \lambda\|\mathbf{S}\|_1 \quad \text{s.t. } \text{rank}(\mathbf{L}) = K \quad (1)$$

$$\mathbf{L}^{(t+1)} = \arg\min_{\mathbf{L}} \|\mathbf{L} + \mathbf{S}^{(t)} - \mathbf{E}\|_F \quad \text{s.t. rank}(\mathbf{L}) = K \quad (2)$$

$$\mathbf{S}^{(t+1)} = \arg\min_{\mathbf{S}} \|\mathbf{L}^{(t+1)} + \mathbf{S} - \mathbf{E}\|_F + \lambda\|\mathbf{S}\|_1 \quad (3)$$

In each (t) iteration, the Eq. (2) is updated with rank $= K$. If $\frac{u_K}{\sum_{i=1}^{K} u_i} > \epsilon$, where u denotes the singular values and ϵ is a small threshold, then the rank is increased by one (i.e., $K = K+1$) and the Eq. (3) is updated too. To update the Eq. (2), a partial SVD$(\mathbf{E}-\mathbf{S}^{(t)})$ is estimated keeping K components. To update the Eq. (3), a shrinkage operator is used $\mathcal{D}(.)$, where:

$$\mathcal{D}(\mathbf{E}-\mathbf{L}^{(t+1)}, \lambda) = \text{sign}(\mathbf{E}-\mathbf{L}^{(t+1)})\max\{0, |\mathbf{E}-\mathbf{L}^{(t+1)}|-\lambda\} \quad (4)$$

C. Guided Normals

Guided normals have been successfully applied in feature-aware mesh approaches [25]–[27]. For each face f_i, a set $\mathcal{B}_i = \{\mathcal{P}_{i1}, \mathcal{P}_{i2}, \ldots, \mathcal{P}_{in_p}\}$ of n_p candidate patches $\mathcal{P}_{ij}$ are estimated. Each patch represents a small area consisting of k neighboring faces, such as $\mathcal{P}_i = \{f_i, f_{i_1}, f_{i_2}, \cdots, f_{i_k}\}$ (including the face f_i). The k geometrical nearest faces of the face f_i are estimated by the k nearest neighbors (k-nn) algorithm (where we set $k = 25$). The main purpose is to find which one of these candidate patches $\mathcal{P}_{ij}$ is the ideal representative area for the face f_i, in terms of the direction of the centroid normals. The parameters that are investigated for the identification of the optimal patch are: (i) the maximum distance between the i centroid normal and the other centroid normals of the same patch (see Eq. (6)) and (ii) the mean saliency ϕ_{ij} based on the salient weights s of a patch $\mathcal{P}_{ij}$ (see Eq. (7)). Among all candidate patches, the ideal-selected patch is the one $\mathcal{P}^*$ with the smallest value of Eq. (5):

$$\mathcal{P}_i^* = (\mathcal{P}_{ij} \mid \min(\omega_{ij}\phi_{ij})) \quad (5)$$

$$\omega_{ij} = \max(\|\mathbf{n}_{ci} - \mathbf{n}_{cl}\|_2) \quad \forall \mathbf{n}_{cl} \in \mathcal{P}_{ij} \quad (6)$$

$$\phi_{ij} = \frac{\sum_{\forall l \in \mathcal{P}_{ij}} s_l}{|\mathcal{P}_{ij}|} \quad (7)$$

$\forall i = 1, \cdots, n_f, \ \forall j = 1, \cdots, n_p$. Examining Eq. (5), we can observe that the ideal patch has a similar direction of normals (small distance ω between normals) and lies in a flat surface area (the smaller the mean saliency ϕ the less the salient features). Finally, the guided normal $\mathbf{g}_i$ is estimated as the weighted average normal of this ideal patch $\mathcal{P}_i^*$:

$$\mathbf{g}_i = \frac{\sum_{f_i \in \mathcal{P}_i^*} A_j \mathbf{n}_{cj}}{\left\|\sum_{f_i \in \mathcal{P}_i^*} A_j \mathbf{n}_{cj}\right\|_2} \quad \forall i = 1, \cdots, n_f \quad (8)$$

where A_j represents the area of face f_j.

IV. OVERVIEW OF OUR METHOD

Fig. 1 briefly presents the pipeline of our approach. We start by separating the whole mesh into n_f (i.e., equal to the number of centroids) overlapped and equally-sized patches. Then, we estimate the spectral and geometrical saliency and finally, we combine these two values. Once the saliency mapping of a mesh has been estimated, it can be used in several different industrial applications, facilitating several processes in manufacturing, maintenance, inspection and repairing.
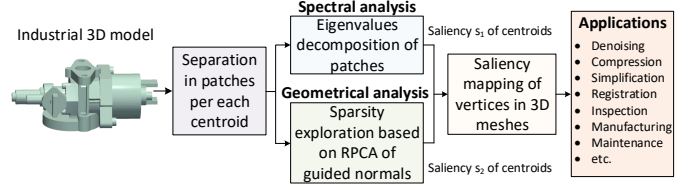

Fig. 1: Pipeline of the proposed method for the estimation of the saliency mapping of 3D meshes based on spectral and geometrical analysis.

A. Geometry-Based Saliency Analysis

The geometrical saliency features are estimated by exploiting the sparsity of the guided normals. Centroid normals $\mathbf{n}_c$ can be also used in this analysis, however, guided normals have a more robust behavior in the presence of scanning noise [27]. The estimated patches $\mathcal{P}_i$ are used for the construction of matrix $\mathbf{E} \in \mathbb{R}^{3n_f \times (k+1)}$:

$$\mathbf{E} = \begin{bmatrix} \mathbf{g}_1 & \mathbf{g}_{11} & \mathbf{g}_{12} & \cdots & \mathbf{g}_{1k} \\ \mathbf{g}_2 & \mathbf{g}_{21} & \mathbf{g}_{22} & \cdots & \mathbf{g}_{2k} \\ \vdots & \vdots & \vdots & \ddots & \vdots \\ \mathbf{g}_{n_f} & \mathbf{g}_{n_f1} & \mathbf{g}_{n_f2} & \cdots & \mathbf{g}_{n_fk} \end{bmatrix} \quad (9)$$

where $\mathbf{g}_i = [g_{i_x}, g_{i_y}, g_{i_z}]^T$. Then, we apply the RPCA approach to this matrix, as described in III-B, taking advantage of the geometrical coherence between neighboring guided normals. By the decomposition, the low-rank $\mathbf{L}$ and sparse $\mathbf{S}$ matrices are estimated. However, the estimation of the geometric saliency feature s_{1i} of the centroid $\mathbf{c}_i$ requires only the values of the first column of the sparse matrix, according to:

$$s_{1i} = \sqrt{S_{i1_x}^2 + S_{i1_y}^2 + S_{i1_z}^2} \quad \forall i = 1, \cdots, n_f \quad (10)$$

where S_{i1_x} denotes the scalar value of the x coordinate, of the ith row, of the 1st column, of the $\mathbf{S}$ matrix.

The motivation for exploiting the sparsity of the guided normals is based on the observation that the similarity of the normals between neighboring triangles is an index of geometrical coherence of the triangles. Low values of the sparse matrix mean that the normals of a triangle and its neighbors are similar (low-rank), so if all triangles of a neighboring area have similar geometrical behavior this means that this patch represents a flat area. On the other hand, if there is a big dissimilarity this means that the surface has an abnormal shape.

B. Spectral-Based Saliency Analysis

For each face f_i of the mesh, we use $\mathbf{E}_i \in \mathbb{R}^{3 \times (k+1)}$, representing the i row of the matrix $\mathbf{E}$ in Eq. (9):

$$\mathbf{E}_i = \begin{bmatrix} g_{ix} & g_{ix_1} & g_{ix_2} & \cdots & g_{ix_k} \\ g_{iy} & g_{iy_1} & g_{iy_2} & \cdots & g_{iy_k} \\ g_{iz} & g_{iz_1} & g_{iz_2} & \cdots & g_{iz_k} \end{bmatrix} \quad \forall i = 1, \cdots, n_f \quad (11)$$

$\mathbf{E}_i$ is used for the estimation of the covariance matrices $\mathbf{R}_i$:

$$\mathbf{R}_i = \mathbf{E}_i\mathbf{E}_i^T \in \mathbb{R}^{3 \times 3} \quad (12)$$

Then, $\mathbf{R}_i = \mathbf{U}\mathbf{\Lambda}\mathbf{U}^T$ is decomposed to a matrix $\mathbf{U}$, consisting of the eigenvectors, and a diagonal matrix $\mathbf{\Lambda} =$

diag$(\lambda_{i1}, \lambda_{i2}, \lambda_{i3})$, consisting of the corresponding eigenvalues $\lambda_{ij}, \forall j = 1 - 3$. Finally, the spectral saliency s_{2i} of a centroid $\mathbf{c}_i$ is denoted as the value given by the inverse l^2-norm of the corresponding eigenvalues:

$$s_{2i} = \frac{1}{\sqrt{\lambda_{i1}^2 + \lambda_{i2}^2 + \lambda_{i3}^2}} \ \forall \ i = 1, \cdots, n_f \quad (13)$$

Observing the Eq. (13), we can see that large values of the term $\sqrt{\lambda_{i1}^2 + \lambda_{i2}^2 + \lambda_{i3}^2}$ correspond to small saliency features indicating that the centroid lies in a flat area, while small values correspond to large saliency values, characterizing the specific centroid as a feature. This can be easily justified by the fact that the centroid normal of a face lying in a flat area is represented by one dominant eigenvector, the corresponding eigenvalue of which has a very large value. On the other hand, the centroid normal of a face lying in a corner is represented by three eigenvectors, that correspond to eigenvalues with small but almost equal amplitude.

C. Estimating the Saliency of Vertices

We then normalize spectral and geometric saliency in a range [0-1], according to:

$$\bar{s}_{ji} = \frac{s_{ji} - \min(s_{ji})}{\max(s_{ji}) - \min(s_{ji})} \ \forall \ i = 1, \cdots, n_f, \ \ j \ \in \{1, 2\} \quad (14)$$

For the sake of completeness, we denote the saliency mapping as the weighted combination of the normalized geometrical $\bar{s}_1$ and spectral $\bar{s}_2$ saliency features, according to:

$$s_{ci} = \frac{w_1 \bar{s}_{1i} + w_2 \bar{s}_{2i}}{w_1 + w_2} \ \ \forall \ i = 1, \cdots, n_f \quad (15)$$

where w_1 and w_2 are the corresponding weights which can be tuned for giving emphasis to the one or the other approach. However, we suggest the use of $w_1 = w_2 = 1$ which are also used in all of our experiments.

The proposed method is robust, even when we assume complex surfaces with different geometrical characteristics, since it exploits spectral characteristic (i.e., over-sensitivity in the variation of neighboring centroid normals) and geometrical characteristics (i.e., sparsity property of intense features). For the estimation of the saliency value of each vertex we use the following equation:

$$s_i = \frac{\sum_{\forall \mathbf{c}_j \in \mathcal{N}_i} s_{cj}}{|\mathcal{N}_i|} \ \ \forall \ i = 1, \cdots, n \quad (16)$$

where $\mathcal{N}_i$ represents the first-ring area of the vertex $\mathbf{v}_i$.

D. Speed up Process - Sampling Matrix $\mathbf{E}$

Besides the fact that we use a very fast variants of RPCA, the most time-consuming step, still is the decomposition of the coherent matrix $\mathbf{E}$ into a low-rank and a sparse matrix. The computational complexity of this method is related to the size of the data, so an approach to decrease the execution time is to use without of course reducing the detection accuracy. To achieve this, we firstly use the saliency mapping results of the spectral method. The salient map helps us to make a first coarse estimation about where the sharp features and the flat areas exist.

We start by assuming that each vertex can be categorized into a saliency class, based on its salient value that has been extracted by the spectral method only. We use 64 classes in total which is equal to the number of different colors of the "jet" colormap that is also used for the visualization of the saliency mapping. Class 1 consists of the least salient vertices, while class 64 consists of the most salient vertices. Then, we are based on the observation that a large quantity of vertices belongs to class 1 (as we can also see in the Histograms of Fig. 2) and we exclude these vertices. Finally we create a smaller dimension matrix $\mathbf{E}' \in \mathbb{R}^{3n'_f \times (k+1)}$ using all the vertices of the rest of the classes [2-64] where $n'_f < n_f$.
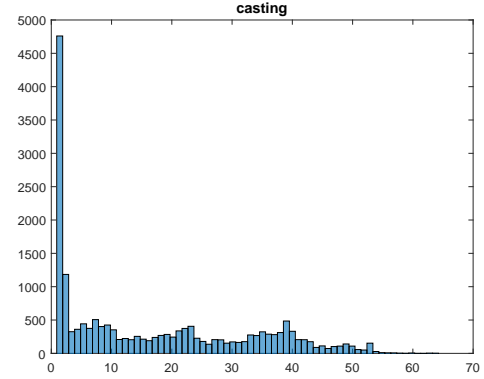

Fig. 2: *Histograms showing the number of vertices per each class. We have used 64 bins equal to the number of colors of the "jet" colormap.*

The final execution times of the fast approach are further improved and the speed up of the new algorithm is up to $\sim 85\%$, as we can see in the Table I. It is also presents the results of the saliency mapping in different models using the two presented approaches, namely the original RPCA and the faster approach applied only to the salient vertices of the mesh. As we can observe, there is no big perceptual difference between the two results.

E. Utilizing 3D Saliency Mapping in Industrial Applications

In the following sub-paragraphs, we present indicatively some industrial applications in which the proposed saliency mapping can be utilized, facilitating several visual tasks.

1) Utilization in the manufacturing industry for quality control inspections: It is very common, in the manufacturing industry, objects to be produced in different sizes, retaining however the same form with the prototype model. Nonetheless, to assure quality, the reconstructed objects must satisfy a range of statutory and contractual obligations. In this case, inspection is used to verify and certify that the new scaled object has been manufactured in full compliance with all specified requirements and constraints. In Fig. 3, we present examples of inspection between real-scanned industrial objects, denoted as prototype models[1][2][3] (Fig. 3-(a)), and their corresponding

[1]"Aeronautics actuator casting" model
[2]"Automobile Hubcap" model
[3]"Oil pump" model

| Model	Number of vertices belongs to category 1	Total number of Vertices	Execution times using the original approach (sec)	Execution times using the fast approach (sec)	Speed up
fandisk	2782	6475	0.46	0.19	59.7 %
cad	8735	19398	1.22	0.42	65.2 %
block	2062	8771	0.38	0.22	40.3 %
joint	15848	20902	1.40	0.34	76.1 %
part_Lp	898	4261	0.31	0.15	50.1 %
coverrear_Lp	4902	7872	0.86	0.13	85.2 %
rockerarm	1782	9413	0.53	0.30	43.1 %
casting	4760	18410	1.14	0.21	81.8 %
trim-star	1806	5192	0.23	0.13	42.0 %
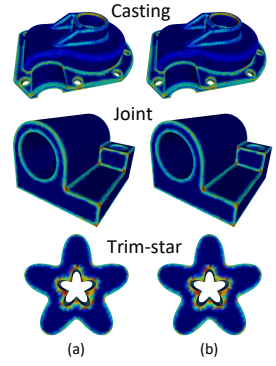
TABLE I: *[Left] Execution times for the original approach and the fast approach using a smaller coherency matrix. [Right] Heat map visualization of the salient map extracted by the (a) Original approach, (b) faster approach applied only to the salient vertices of the mesh.*

scaled and deformed 3D objects (Fig. 3-(b)). Our purpose is to inspect if the new manufactured 3D object has the exact same design details as the original (regarding the fidelity of its form) and also to ensure that it has not been affected by irregularities encountered during the manufacturing processes. In Fig. 3-(c), we present an enlarged representation of the scaled model, presented in Fig. 3-(b), with red cycles that specify the deformed areas. The purpose of this application is to automatically identify deformations or other abnormalities from the surface of the manufactured 3D object in comparison with the original model. For easier comparison, we provide a heatmap visualization of the difference between the original and the constructed model. Blue color means that there is no difference between the compared models while red color indicates a big difference. Our method is able to find and highlight possible differences between two objects with similar shapes comparing the saliency values of their surface. In this way, it is capable to automatically inspect degradations of the surface standards of manufactured objects despite the constraints posed by scaled manufactured objects or objects created by different materials. For the comparisons between the original and the reconstructed models, we used two different approaches. In the first approach, we deployed the Hausdorff distance (HD) (Fig. 3-(d)) of the normalized models (with values in the range [0-1]) while in the second approach, we used both HD and the salient values (Fig. 3-(e)) according to Eq. (16). We assume that we have two normalized 3D models $\mathcal{M}_1 \in \mathbb{R}^{n_1 \times 3}$ and $\mathcal{M}_2 \in \mathbb{R}^{n_2 \times 3}$, where $n_1 \neq n_2$ (e.g., original and compared respectively). Firstly, for each vertex of the these two models, we create a representative vector consisting of the values of its coordinates and its saliency:

$$\mathbf{q}_{ji} = [\mathbf{v}_{ji} \ s_{ji}] \in \mathbb{R}^{4 \times 1} \quad (17)$$

$\forall \ j \in \{1, 2\}, i \in [1, \cdots, n_1], \ [1, \cdots, n_2]$. Then, for each i vertex of $\mathcal{M}_2$ we find the closest d_i^* vertex of $\mathcal{M}_1$ based on their norm 2 difference:

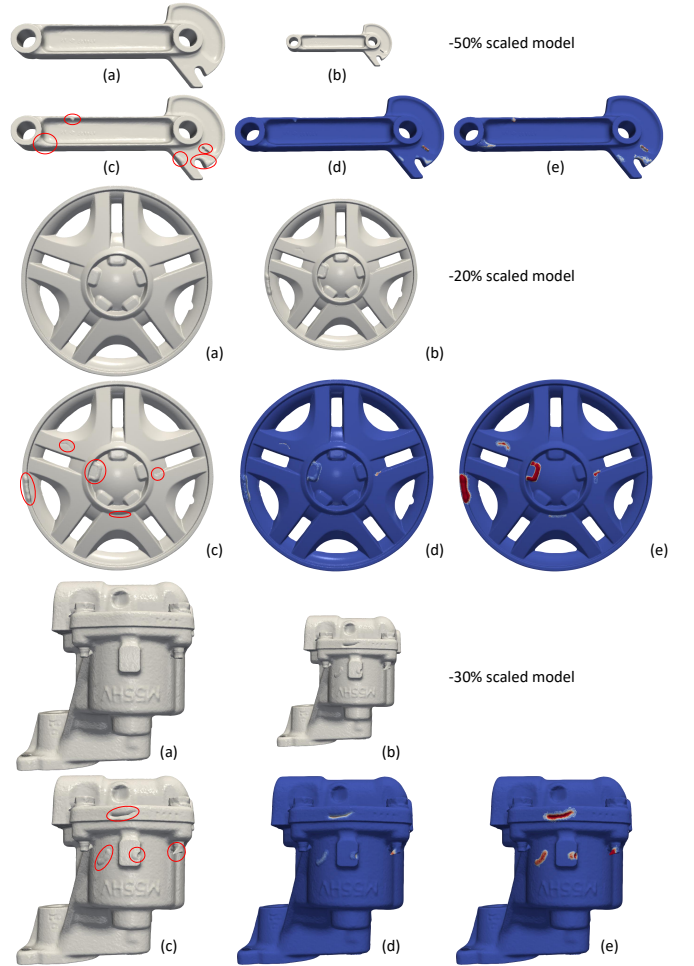$$d_i^* = \arg\min_{d} D(\mathbf{q}_{2i}, \mathbf{q}_{1d}) \ \forall \ d \in [1, \cdots, n_1] \quad (18)$$

Fig. 3: [**First line**] (a) Original models, (b) scaled and deformed models. [**Second line**] Enlarged representations of (b) with: (c) red cycles for highlighting the deformed areas, (d) heatmap visualization of HD applied to vertices, (e) heatmap visualization of HD applied both to vertices and salient values.
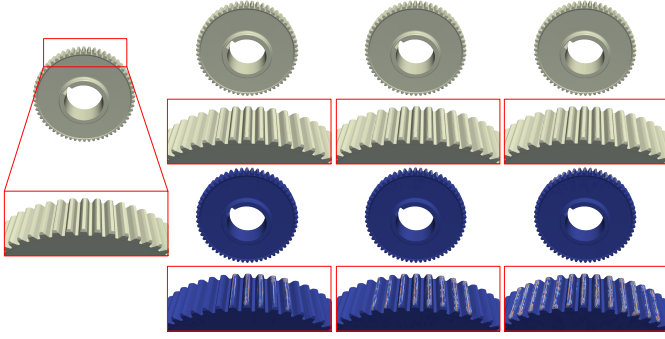
Fig. 4: Digital twin of gear model in a early stage and after 3 consecutive temporal moments.

$\forall i \in [1, \cdots, n_2]$), where:

$$D(\mathbf{q}_2, \mathbf{q}_1) = \sqrt{(x_2 - x_1)^2 + (y_2 - y_1)^2 + (z_2 - z_1)^2 + (s_2 - s_1)^2} \quad (19)$$

Then for these indices d_i^*, we estimate the saliency difference $(s_{2i} - s_{1d_i^*}) \ \forall \ i = 1, \cdots, n_2$ and we visualize it. The experiments verifies that the proposed approach can identify deviations easily and with great detail.

2) Utilization for the creation of digital twins and aging inspection: The proposed method supports detecting changes that can be caused by aging, comparing the saliency mapping of a 3D object having been acquired in two or more different temporal moments. In this way, our approach could be used to identify surface differences of the same object, affected by mechanical stress (e.g., a gear of a machine) or deteriorated due to environmental conditions (e.g., an ancient statue or columns). In Fig. 4, we present visual representations of the same gear in 4 different occasions (i.e., in a early stage and after 3 consecutive temporal moments). This figure shows that our method is able to capture differences due to aging, so indiscernible, that even the human eye could not easily notice.

3) Utilization in the heritage industry for the maintenance of the historical objects: In Fig. 5, we present examples of real-scanned historical objects [4] [5] in which the proposed method of the saliency mapping can be utilized so as to automatically detect cracks and other defects on their surfaces. The presented figures verify that the proposed 3D saliency mapping approach is very useful since it can be used for identifying areas of the original model that need to be repaired, facilitating the work of the experts during the maintenance process. Our method uses small patches of neighboring vertices, thus if an abnormality appears somewhere in the surface, then our algorithm is able to recognize it and highlight this specific area. The higher the abnormality, the higher the value of salience, so it is ideal for inspection of cracks, damages, etc,. In this way, this method could be used as a pre-processing step for the creation of a digital replica of the original cultural object, without imperfections, since it highlights the areas that need repair (i.e., digital repairing is also available). The recent

---

[4]"Calcite Vase" model
[5]"Epichysis 26332 b" model
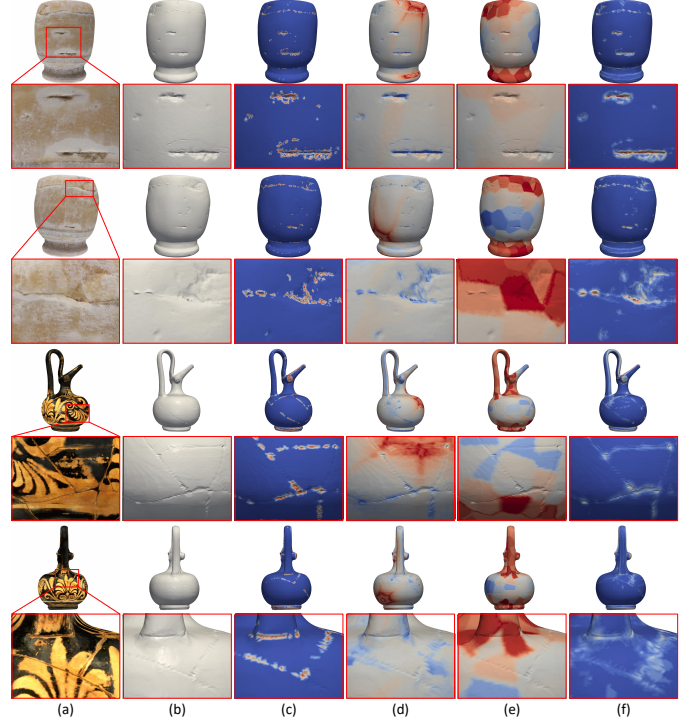

(a)   (b)   (c)   (d)   (e)   (f)

Fig. 5: Original model (a) with texture, (b) with no texture. Heatmap visualization of saliency mapping using: (c) curvature co-occurrence histogram [9], (d) entropy based salient model [11], (e) mesh saliency via spectral processing [12], (f) the proposed method.

trend for digitalization and creation of digital twin models has a lot of historical interest in the heritage industry. A digital repaired 3D model can be used for the VR/AR representation of a heritage object (e.g., for educational purposes) showing how it looked like originally and additionally giving to the visitors the opportunity to see reconstructed views of the object.

V. EXPERIMENTAL ANALYSIS AND RESULTS

The proposed saliency mapping was evaluated using: (a) heatmaps visualization, (b) 3D mesh simplification based on the saliency of the vertices, and (c) a denoising application using the saliency values for finding the ideal patches.

It should be emphasized that, in most cases, there is no ground truth saliency map or a reliable metric that can be used for benchmarking purposes. The typical way to evaluate a saliency map is via subjective evaluation. The subjective evaluation can clearly show if a specific saliency mapping has achieved its purpose, applied in a specific application, and provides a fair comparison with the results of other salient mapping methods.

1) Heatmap Visualization of Saliency Mapping: Fig. 6 presents the heatmap visualization of the 3D saliency mapping applied in different industrial 3D models. For easier comparison, all the results are normalized, taking values [0-1] Eq. (14). The used colormap for the visualization is the "jet" contenting
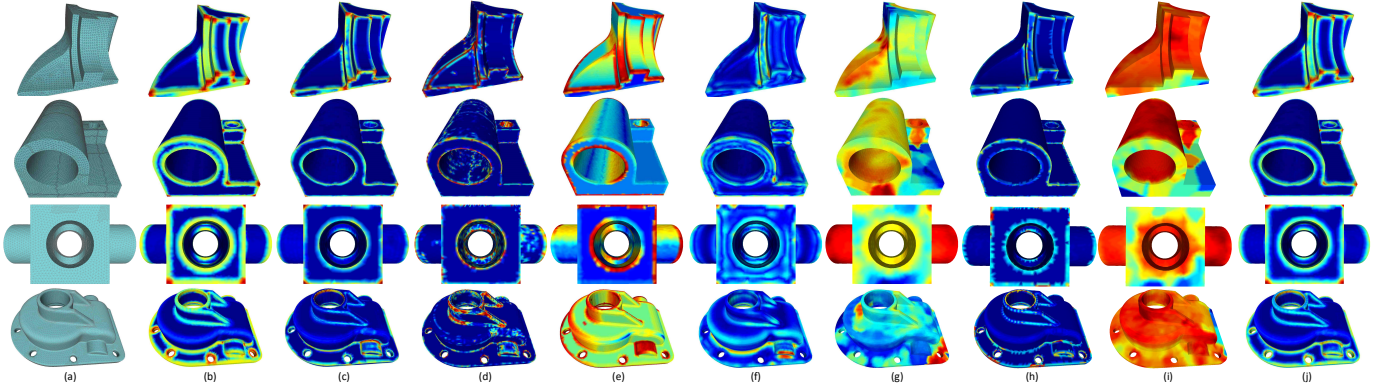
Fig. 6: (a) Original model, and heatmaps visualization of saliency mapping based on: (b) the eigenvalues of small patches (spectral analysis), as described in paragraph IV-B, (c) the RPCA approach (geometrical analysis), as described in paragraph IV-A, (d) Wei *et al.* [9], (e) Tao *et al.* [11], (f) Lee *et al.* [28], (g) Song *et al.* [12], (h) Guo *et al.* [29], (i) Song *et al.* (CNN) [30], (j) our approach.

64 colors (deep blue = 0, deep red = 1). Saliency mapping of a 3D object must provide visual information that can be easily recognizable. This means that different areas with different characteristics will be highlighted with a different color. On the other hand, different areas with the same characteristics will be highlighted with the same color. The experimental results show that our method (in Fig. 6-(e)) successfully follows this direction providing more robust and meaningful results than the other approaches. More specifically, the highest values (red colors) represents very distinctive vertices (e.g., corners), while the lowest values (blue colors) represents flat areas.

2) Simplification Based on the Saliency of Vertices: Due to the easiness of creating digital 3D content nowadays, a great amount of information can be captured and stored. The information, acquired by 3D scanners, is usually huge creating dense 3D models that are very difficult to be efficiently handled by other applications (i.e., high computational complexity). This information must be simplified, keeping only of the most representative information, and removing least important information. Simplification is a low-level application that focus on representing an object using a lower resolution mesh without errors or with errors that cannot be easily perceived. The main objective of a successful simplification approach is to remove only those vertices which do not offer significant geometric information to the simplified 3D object and their removal will not change significantly the shape or perceptual details of the 3D object. Following this line of thought, we suggest to remove the least perceptually important vertices, preserving only the most salient vertices for the reconstruction of the new simplified 3D model. More specifically, the steps of the suggested simplification process are: (i) all vertices are sorted based on their salient values. (ii) The K-th vertices with the higher salient values remain. (iii) the rest $n - K$ less salient vertices are removed and the k-nn algorithm is used for the recreation of the new connectivity (triangulation). Fig. 7 presents simplified meshes under different simplification scenarios.

3) Feature-aware Denoising Based on the Saliency of Vertices: Guided normals filtering has been used in past works [26], [25] providing excellent denoising results. In [26], the saliency is estimated by using the difference between the normals of the two incident faces.

We follow the same line of thought but we use a different way for the estimation of the ideal patch. More specifically, we select the patch that has the smallest value of Ψ, according to Eqs. (20)-(21), since it consists of "less salient" faces (flat areas that are depicted with deep blue color).

$$\mathcal{P}_i^* = (\mathcal{P}_{ij} \mid \min(\Psi_{ij})) \ \ \forall \ i = 1, \cdots, n, j = 1, \cdots, n_p \quad (20)$$

$$\text{where} \quad \Psi_{ij} = \frac{\sum_{\forall l \in \mathcal{P}_{ij}} s_l}{|\mathcal{P}_{ij}|} \ \ \forall \ l = 1, \cdots, k \quad (21)$$

In Fig. 8, we present an example of five candidate patches (for the face which is depicted by the yellow normal). In these examples, we show that the selected ideal patch is this one with the lowest value of Ψ (i.e., $\Psi = 0.32$ and $\Psi = 0.37$), representing the area with the less salient features. As we can observe, both the first and the last patches represent totally flat areas, however they do not have the same Ψ value since the first patch consists of more salient triangles in comparison to the last patch, so the last area is more preferable to represent the ideal patch. We also can observe that our method provides reliable results of saliency mapping even under the presence of noise, which makes it ideal for use in applications with noisy 3D models. The purpose of this example is the estimation of the most representative centroid normal (i.e., guided normal) in order to use it for a more efficient bilateral filtering [31]:

$$\mathbf{W}_{1_{ij}} = \exp(\frac{-\|\mathbf{c}_i - \mathbf{c}_j\|^2}{2\sigma_1^2}), \quad \mathbf{W}_{2_{ij}} = \exp(\frac{-\|\mathbf{g}_i - \mathbf{g}_j\|^2}{2\sigma_2^2}) \quad (22)$$

$$\hat{\mathbf{n}}_c = \frac{\sum_{f_j \in \mathcal{P}_i} A_j \mathbf{W}_{1_{ij}} \mathbf{W}_{2_{ij}} \mathbf{n}_{cj}}{\|A_j \mathbf{W}_{1_{ij}} \mathbf{W}_{2_{ij}} \mathbf{n}_{cj}\|_2} \quad (23)$$
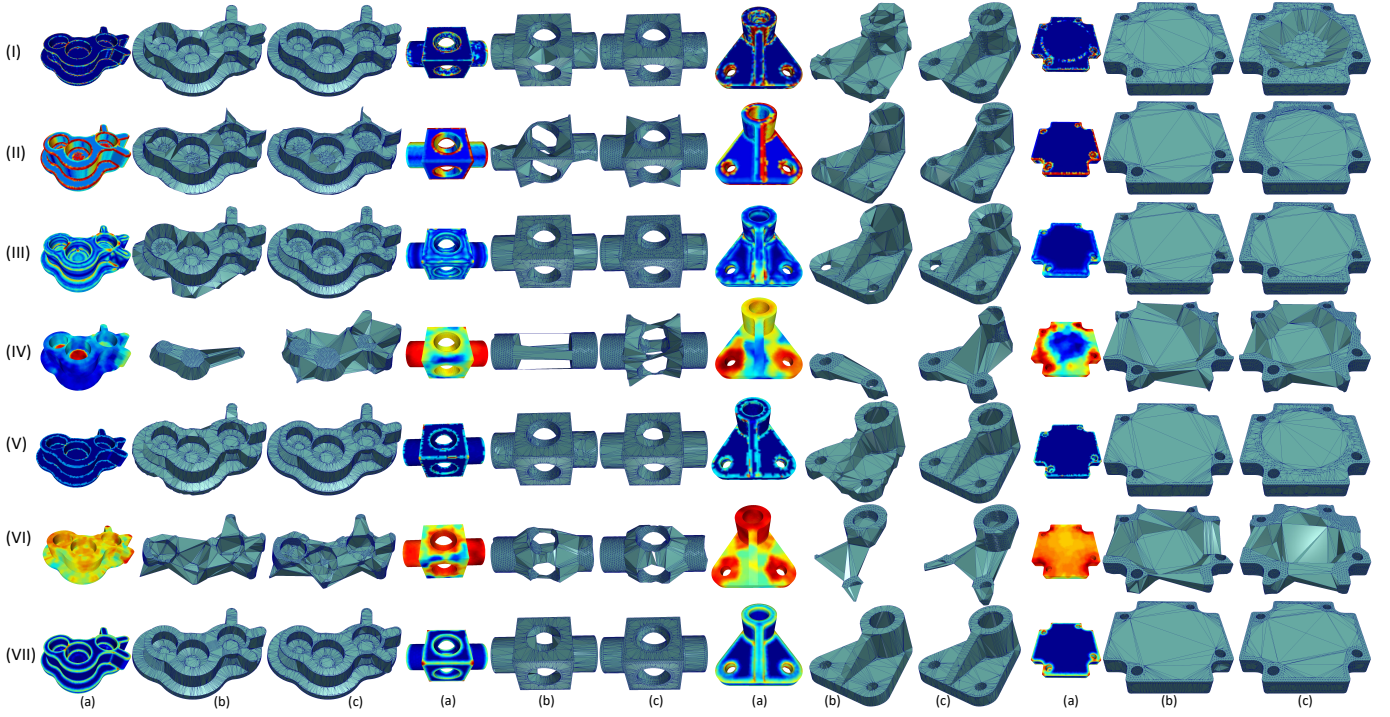
Fig. 7: *Simplification of 3D models using the saliency mapping of different methods, namely: (I) Wei et al. [9], (II) Tao et al. [11], (III) Lee et al. [28], (IV) Song et al. [12], (V) Guo et al. [29], (VI) Song et al. (CNN) [30] and (VII) our approach respectively (from up to down). (a) Heatmap visualization of the saliency mapping and simplified results using different simplification approaches,* **Cad** *(19,398 points): (b) 2000 ($\sim$ 10.3%), (c) 4000 ($\sim$ 20.6%),* **Block** *(8,771 points): (b) 2000 ($\sim$ 22.8%), (c) 4000 ($\sim$ 45.6%),* **Part Lp** *(4,261points): (b) 500 ($\sim$ 11.7%), (c) 1000 ($\sim$ 23.4%),* **Coverrear Lp** *(7,872 points): (b) 2000 ($\sim$ 25.4%), (c) 3000 ($\sim$ 38.1%).*
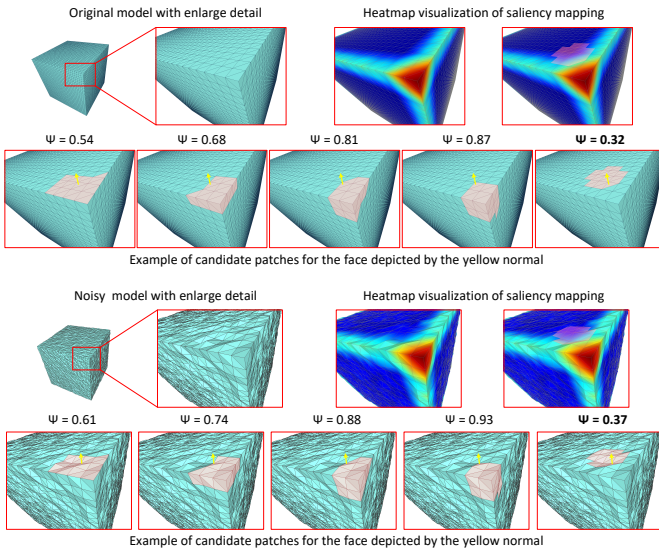

Fig. 8: Ideal patch selection based on the proposed saliency mapping.

Finally, the denoised normals $\hat{\mathbf{n}}_c$ are used to update the vertices according to [32]:

$$\mathbf{v}_i = \mathbf{v}_i + \frac{\sum_{\mathbf{c}_j \in \mathcal{N}_i} \hat{\mathbf{n}}_{cj}(\langle \hat{\mathbf{n}}_{cj}, (\mathbf{c}_j - \mathbf{v}_i) \rangle)}{|\mathcal{N}_i|} \qquad (24)$$

where $\langle \mathbf{a}, \mathbf{b} \rangle$ represents the inner product of $\mathbf{a}$ and $\mathbf{b}$. Note here that we do not search for ideal parameters per each 3D model or method. Instead, in all the experiments and for any of the approaches, we use exactly the same values for each parameter. Specifically, we define $\sigma_2 = 0.25$, $\sigma_{1_{ij}} = \sum_{\forall \mathbf{c}_j \in \mathcal{N}_i} \|\mathbf{c}_i - \mathbf{c}_j\|_2^2 / |\mathcal{N}_i|$ [31], 15 iterations for the bilateral filtering Eqs. (22)-(23) and 20 iterations for the vertex updating Eq. (24). The ideal selected patch must consist of normals with similar direction (in order to satisfy the normals' consistency). The patches that have a lot of corners or edges must be banned (i.e., high salient values in our case) since they consist of normals lying in different directions. As a result, the value of Ψ would be totally misleading since it would not represent a specific planar area. Fig. 9 presents the denoising results with enlarged regions for easier comparisons. The quality of the reconstructed models is evaluated using the metrics: (i) θ representing the mean angle between the normals of the ground truth and the reconstructed faces and (ii) the Hausdorff distance (HD).
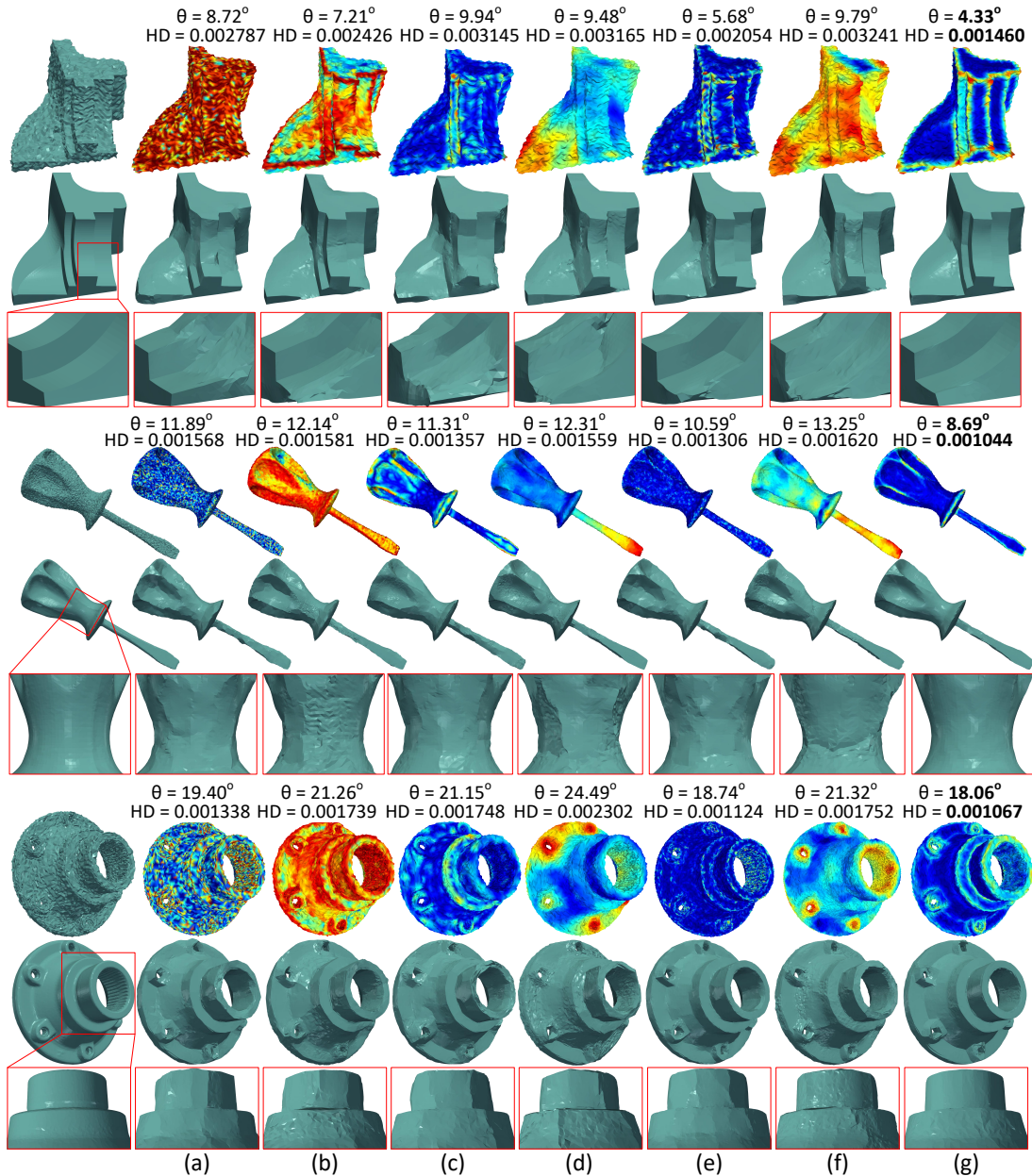
Fig. 9: Heatmaps of saliency mapping and denoising results using the methods: (a) curvature co-occurrence histogram [9], (b) entropy based salient model [11], (c) a mesh saliency [28], (d) mesh saliency via spectral processing [12], (e) Point-wise saliency detection [29], (f) mesh saliency via CNN [30], (g) our approach.

VI. CONCLUSIONS AND DISCUSSION

We presented a 3D feature-aware saliency estimation approach, taking into account both spectral and geometrical information of a 3D object. Purpose of this research is to provide a meaningful 3D saliency mapping which could be beneficial for industrial applications. Extensive evaluation studies, carried out with several evaluation scenarios (e.g., heatmap visualization for visual perception, simplification, denoising), verify the superiority of our approach as compared to other state-of-the-art approaches. We also presented a variety of actual industrial applications (i.e., manufacturing

inspection of scaled object, inspection of aging mechanical parts, facilitation of heritage repairing/maintenance) in which our method can be successfully utilized, in different industrial areas (i.e., manufacturing, heritage, medical).

The saliency mapping of our method does not just detect defects, but it highlights areas with high-frequency spatial components (which means sharp features, noise, and abnormalities) and areas where a neighborhood of normals have a random variance behavior (normals of this neighborhood do not have a prevailing direction). In other words, our approach highlights areas where the range distribution of normals is

high. In the following Fig. 10, we present boxplots showing the standard deviation of the normals for all overlapped patches which have been categorized (into 8 categories) based on the salient values of each vertex. More specifically, we estimate the standard deviation of the normals of each patch $\mathbf{E}_i \ \forall \ i = 1, \cdots, n$:

$$\sigma_i = \text{std}(\mathbf{E}_i) \ \forall \ i = 1, \cdots, n_f \tag{25}$$

where std(A) represents the equation that estimates the standard deviation of the values consisting of A. Then, we categorize each vertex based on the saliency values of our method in 8 categories.

As we can see, categories consisting of less salient vertices, representing flat areas, have smaller mean values of standard deviation since all the normals of a neighborhood have a common direction and form. On the other hand, as we move to categories including more salient vertices, the mean value of the standard deviation increases, meaning that the directions of the normals of a neighborhood become more irregular.
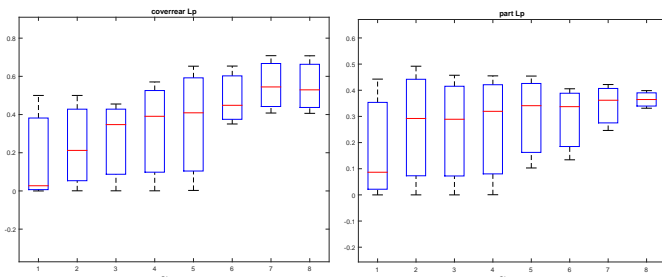

Fig. 10: *Boxplot of standard deviation of normals per different classes.*

REFERENCES

[1] S. von Enzberg and A. Al-Hamadi, "A multiresolution approach to model-based 3-d surface quality inspection," *IEEE Transactions on Industrial Informatics*, vol. 12, no. 4, pp. 1498–1507, Aug 2016.

[2] C. Piciarelli, D. Avola, D. Pannone, and G. L. Foresti, "A vision-based system for internal pipeline inspection," *IEEE Transactions on Industrial Informatics*, vol. 15, no. 6, pp. 3289–3299, June 2019.

[3] Z. Jakovljevic, R. Puzovic, and M. Pajic, "Recognition of planar segments in point cloud based on wavelet transform," *IEEE Transactions on Industrial Informatics*, vol. 11, no. 2, pp. 342–352, April 2015.

[4] F. Tao, H. Zhang, A. Liu, and A. Y. C. Nee, "Digital twin in industry: State-of-the-art," *IEEE Transactions on Industrial Informatics*, vol. 15, no. 4, pp. 2405–2415, April 2019.

[5] Y. Wang, W. Xiong, J. Cheng, S. C. Chia, W. Chen, W. Huang, and J. Zhou, "Vision based hole crack detection," in *2015 IEEE 10th Conference on Industrial Electronics and Applications (ICIEA)*, June 2015, pp. 1932–1936.

[6] I. Abouelaziz, A. Chetouani, M. E. Hassouni, L. J. Latecki, and H. Cherifi, "Convolutional neural network for blind mesh visual quality assessment using 3d visual saliency," in *2018 25th IEEE International Conference on Image Processing (ICIP)*, Oct 2018, pp. 3533–3537.

[7] X. Ding, W. Lin, Z. Chen, and X. Zhang, "Point cloud saliency detection by local and global feature fusion," *IEEE Transactions on Image Processing*, vol. 28, no. 11, pp. 5379–5393, Nov 2019.

[8] X. Liu, P. Tao, J. Cao, H. Chen, and C. Zou, "Mesh saliency detection via double absorbing markov chain in feature space," *The Visual Computer*, vol. 32, no. 9, pp. 1121–1132, Sep 2016. [Online]. Available: https://doi.org/10.1007/s00371-015-1184-x

[9] N. Wei, K. Gao, R. Ji, and P. Chen, "Surface saliency detection based on curvature co-occurrence histograms," *IEEE Access*, vol. 6, pp. 54 536–54 541, 2018.

[10] S. Lu, C. Tan, and J. Lim, "Robust and efficient saliency modeling from image co-occurrence histograms," *IEEE Transactions on Pattern Analysis and Machine Intelligence*, vol. 36, no. 1, pp. 195–201, Jan 2014.

[11] P. Tao, L. Zhang, J. Cao, and X. Liu, "Mesh saliency detection based on entropy," in *2016 6th International Conference on Digital Home (ICDH)*, Dec 2016, pp. 288–295.

[12] R. Song, Y. Liu, R. R. Martin, and P. L. Rosin, "Mesh saliency via spectral processing," *ACM Trans. Graph.*, vol. 33, no. 1, pp. 6:1–6:17, Feb. 2014. [Online]. Available: http://doi.acm.org/10.1145/2530691

[13] G. An, T. Watanabe, and M. Kakimoto, "Mesh simplification using hybrid saliency," in *2016 International Conference on Cyberworlds (CW)*, Sep. 2016, pp. 231–234.

[14] A. Nouri, C. Charrier, and O. Lzoray, "Full-reference saliency-based 3d mesh quality assessment index," in *2016 IEEE International Conference on Image Processing (ICIP)*, Sep. 2016, pp. 1007–1011.

[15] ——, "Multi-scale saliency of 3d colored meshes," in *2015 IEEE International Conference on Image Processing (ICIP)*, Sep. 2015, pp. 2820–2824.

[16] Y. Zhao, Y. Liu, R. Song, and M. Zhang, "Extended non-local means filter for surface saliency detection," in *2012 19th IEEE International Conference on Image Processing*, Sep. 2012, pp. 633–636.

[17] J. Wu, X. Shen, W. Zhu, and L. Liu, "Mesh saliency with global rarity."

[18] M. Lau, K. Dev, W. Shi, J. Dorsey, and H. Rushmeier, "Tactile mesh saliency," *ACM Trans. Graph.*, vol. 35, no. 4, pp. 52:1–52:11, Jul. 2016. [Online]. Available: http://doi.acm.org/10.1145/2897824.2925927

[19] P. Liu, M. Reale, X. Zhang, and L. Yin, "Saliency-guided 3d head pose estimation on 3d expression models," in *Proceedings of the 15th ACM on International Conference on Multimodal Interaction*, ser. ICMI '13. New York, NY, USA: ACM, 2013, pp. 75–78. [Online]. Available: http://doi.acm.org/10.1145/2522848.2522864

[20] N. Kobyshev, H. Riemenschneider, A. Bdis-Szomor, and L. V. Gool, "3d saliency for finding landmark buildings," in *2016 Fourth International Conference on 3D Vision (3DV)*, Oct 2016, pp. 267–275.

[21] J. Yun and J. Sim, "Supervoxel-based saliency detection for large-scale colored 3d point clouds," in *2016 IEEE International Conference on Image Processing (ICIP)*, Sep. 2016, pp. 4062–4066.

[22] E. J. Candès, X. Li, Y. Ma, and J. Wright, "Robust principal component analysis?" *Journal of the ACM (JACM)*, vol. 58, no. 3, p. 11, 2011.

[23] Z. Lin, M. Chen, and Y. Ma, "The augmented lagrange multiplier method for exact recovery of corrupted low-rank matrices," *CoRR*, vol. abs/1009.5055, 2009.

[24] P. Rodrguez and B. Wohlberg, "Fast principal component pursuit via alternating minimization," in *2013 IEEE International Conference on Image Processing*, Sep. 2013, pp. 69–73.

[25] G. Arvanitis, A. S. Lalos, K. Moustakas, and N. Fakotakis, "Feature preserving mesh denoising based on graph spectral processing," *IEEE Transactions on Visualization and Computer Graphics*, vol. 25, no. 3, pp. 1513–1527, March 2019.

[26] W. Zhang, B. Deng, J. Zhang, S. Bouaziz, and L. Liu, "Guided mesh normal filtering," *Computer Graphics Forum (Special Issue of Pacific Graphics 2015)*, vol. 34, pp. 23–34, 2015.

[27] A. S. Lalos, G. Arvanitis, A. Spathis-Papadiotis, and K. Moustakas, "Feature aware 3d mesh compression using robust principal component analysis," in *2018 IEEE International Conference on Multimedia and Expo (ICME)*, July 2018, pp. 1–6.

[28] C. H. Lee, A. Varshney, and D. W. Jacobs, "Mesh saliency," in *ACM SIGGRAPH 2005 Papers*, ser. SIGGRAPH '05. New York, NY, USA: ACM, 2005, pp. 659–666. [Online]. Available: http://doi.acm.org/10.1145/1186822.1073244

[29] Y. Guo, F. Wang, and J. Xin, "Point-wise saliency detection on 3d point clouds via covariance descriptors," *Vis. Comput.*, vol. 34, no. 10, p. 13251338, Oct. 2018. [Online]. Available: https://doi.org/10.1007/s00371-017-1416-3

[30] R. Song, Y. Liu, and P. Rosin, "Mesh saliency via weakly supervised classification-for-saliency cnn," *IEEE Transactions on Visualization and Computer Graphics*, pp. 1–1, 2019.

[31] Y. Zheng, H. Fu, O. K. Au, and C. Tai, "Bilateral normal filtering for mesh denoising," *IEEE Transactions on Visualization and Computer Graphics*, vol. 17, no. 10, pp. 1521–1530, Oct 2011.

[32] X. Sun, P. L. Rosin, R. R. Martin, and F. C. Langbein, "Fast and effective feature-preserving mesh denoising," *IEEE TRANSACTIONS ON VISUALIZATION AND COMPUTER GRAPHICS*, vol. 13, no. 5, p. 925938, 2007.
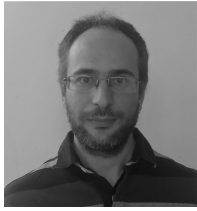
Gerasimos Arvanitis received the Diploma degree in Electrical and Computer Engineering and the M.Sc. degree in electronics and information processing from the University of Patras, Patras, Greece in 2009, and 2011, respectively. From 2011 to 2015, he worked as a software programmer at the Computer Technology Institute in Patras, Greece. He is currently pursuing his Ph.D. degree and he is a member of the Visualization and Virtual Reality Group at the University of Patras since January 2016. He has participated in 4 European projects and he acts as a regular reviewer for several technical journals and conferences. He has authored or co-authored over 25 papers in refereed journals, edited books, and international conferences. His main research interests include digital geometry processing, 3D modeling, reconstruction, compression, outliers removal, feature preserving denoising algorithms, and computer graphics.

Konstantinos Moustakas (Senior Member, IEEE) (M'07–SM'16) received the Diploma degree and the PhD in electrical and computer engineering from the Aristotle University of Thessaloniki, Greece, in 2003 and 2007 respectively. During 2007-2011 he served as a post-doctoral research fellow in the Information Technologies Institute, Centre for Research and Technology Hellas. He is currently an Associate Professor in the Electrical and Computer Engineering Department of the University of Patras, Head of the Visualization and Virtual Reality Group, Director of the Wire Communications and Information Technology Laboratory and Director of the MSc Program on Biomedical Engineering of the University of Patras. His main research interests include virtual, augmented and mixed reality, 3D geometry processing, haptics, virtual physiological human modeling, information visualization, physics-based simulations, computational geometry, computer vision, and stereoscopic image processing. During the latest years, he has been the (co)author of more than 200 papers in refereed journals, edited books, and international conferences. His research work has received several awards. He serves as a regular reviewer for several technical journals and has participated in more than 20 research and development projects funded by the EC and the Greek Secretariat of Research and Technology. He is/was the coordinator of the GameCar H2020 project and scientific coordinator of the NoTremor FP7 project. He has also been a member of the organizing committee of several international conferences. He is a senior member of the IEEE, the IEEE Computer Society and member of Eurographics.

Aris S. Lalos (Senior Member, IEEE) (M'07–SM'19) received his Diploma degree, his M.A.Sc. degree and his Ph.D. from the Computer Engineering and Informatics Department (CEID), School of Engineering (SE), University of Patras (UoP), Rio Patras, Greece in 2003, 2005 and 2010, respectively. He has been a research fellow at Signal Processing and Communications Laboratory, CEID, SE, UoP, Rio-Patras, Greece from 2005 to 2010, in Signal Theory and Communications (TSC) Department of the Technical University of Catalonia (UPC), Barcelona, Spain from Oct. 2012-Dec. 2014 and in the Visualization and Virtual Reality Group from Jan. 2015 until the the present date. In the period Oct. 2011- Oct. 2012 was a telecommunication research engineer at Analogies S.A, an early stage start up. In May 2018, Aris S. Lalos was elected Principal Researcher (Associate Research Professor Level with tenure) at Industrial Systems Institute , ATHENA Research Centre. His general research interest include, digital communications, adaptive filtering algorithms, geometry processing, wireless body area networks and biomedical Signal Processing. He is an author of 96 research papers in international journals (32), conferences (60) and book chapters (4). He has participated in more than 18 European projects related to the ICT and eHealth domain and he acts as a regular reviewer for several technical journals. Aris Lalos received the best demo award in IEEE CAMAD 2014, the best paper award in IEEE ISSPIT 2015, the Worlds FIRST 10K Best Paper Award in IEEE ICME 2017 while, in January 2015, he was nominated as Exemplary Reviewer for the IEEE Communications Letters. He is an IEEE Senior Member since July 2019.